THE ASTROPHYSICAL JOURNAL, 556:896–904, 2001 August 1

OBSERVATIONAL CONSTRAINTS ON CORONAL HEATING MODELS USING CORONAL DIAGNOSTICS SPECTROMETER AND SOFT X-RAY TELESCOPE DATA

J. T. SCHMELZ, R. T. SCOPES, J. W. CIRTAIN, H. D. WINTER, AND J. D. ALLEN
University of Memphis, Physics Department, Memphis, TN 38152; jschmelz@memphis.edu
Received 2000 December 22; accepted 2001 March 30

ABSTRACT

We have constructed a multithermal differential emission measure distribution for several pixels along a relatively isolated coronal loop on the southwest limb of the solar disk using spectral line data from the *Solar and Heliospheric Observatory* coronal diagnostics spectrometer (CDS) and broadband data from the *Yohkoh* soft X-ray telescope. The temperature distributions are clearly inconsistent with isothermal plasma along either the line of sight or the length of the loop. These conclusions disagree with some recent results that used an isothermal approximation derived from narrowband filter ratios to calculate loop temperature profiles. The differences between their results and ours could be attributed to pixel size—CDS pixels are larger, and more "contaminating" material would be expected along the line of sight. To test this idea, we used CDS iron line ratios from our data set to mimic the isothermal results from the narrowband filter instruments. The results gave temperature gradients that were almost flat, indicating that the larger CDS pixel size is not the cause of the discrepancy. A significant intensity was measured for the O v line about 8 scale heights above the limb. In order to account for these observed values, the cool end (below 1 mK) of the emission measure curves must turn up again, even for the pixels at the top of the loop. Plasma densities fell off with loop height producing a relatively constant pressure, and radiative losses were greater than, but did not overwhelm, conductive losses.

Subject headings: Sun: corona — Sun: fundamental parameters

1. INTRODUCTION

The coronal heating problem is unusual in that the theoretical side of the puzzle is well developed while the observational side is woefully inadequate. One approach that has provided some interesting insights is to determine how the heating rate scales with observable physical parameters. These observational and theoretical scaling laws can be compared, and the success (or lack thereof) can be used to evaluate the probability that a particular coronal heating model is working under the conditions examined using the observations. For example, many models predict that the heating rate has a power-law dependence on both the magnetic field strength as well as the length of the field lines. Klimchuk & Porter (1995) find that the heating rate scales as L^{-2} and Mandrini, Démoulin, & Klimchuk (2000) find that $B \propto L^{\delta}$, where $\delta = -0.88 \pm 0.3$. With these results, they find good agreement with models involving the gradual stressing of the magnetic field by slow footpoint motions and not-so-good agreement with wave-heating models. They emphasize, however, that their observational uncertainties must be reduced before they can come to any specific conclusion about a particular heating mechanism.

A second promising avenue of observational investigation of the coronal heating problem has been the height dependence of the heating rate (e.g., Sturrock, Wheatland, & Acton 1996; Kano & Tsuneta 1996). For example, Priest et al. (1998) note that although the overall loop temperature is insensitive to the nature of the coronal heating, the temperature profile along the loop is highly sensitive to the heating mechanism. They measured the temperature profile of an isolated, large-scale loop observed with the soft X-ray telescope (SXT) on *Yohkoh* using the broadband filter ratio method and compared the results with the temperature structure predicted from various coronal heating models, e.g., a uniform heating distribution, a distribution that was localized at the top of the loop, and a distribution that concentrated the heating at the footpoints. Their results favor a uniform heating distribution along the loop, suggesting that neither low-lying heating near the loop footpoints nor summit reconnection was responsible for the heating in this particular loop. They conclude that unless waves can be shown to produce uniform heating, their evidence favors turbulent reconnection at many small randomly distributed current sheets.

Finally, Aschwanden and collaborators have written several papers analyzing data taken with the extreme-ultraviolet imaging telescope (EIT) on board the *Solar and Heliospheric Observatory* (*SOHO*; Aschwanden et al. 1999, 2000). They use a dynamic stereoscopy method to reconstruct the three-dimensional geometry of the observed loops and determine numerous plasma parameters along individual loop segments. Their results show a relatively flat temperature gradient, dT/ds, and therefore a physically insignificant conductive loss rate. In fact, the derived radiative loss rate exceeds the conductive loss rate by about 2 orders of magnitude, implying that the loops cannot be in quasi-static equilibrium. In addition, their results imply that the heating function must be concentrated near the loop footpoints, in direct contrast to the results from Priest et al. (1998, 2000).

In this paper, we combine broadband data from SXT with spectral line data from the coronal diagnostics spectrometer (CDS) on *SOHO* to produce a multithermal distribution—a differential emission measure (DEM) curve—at each of 13 pixels along an isolated coronal loop observed on the southwest limb of the solar disk. In § 2, we describe the observations of the loop made with both instruments, including the calibration and coalignment of the data set. In § 3, we discuss our analysis, including the differences between the isothermal approximations and our DEM distributions, as well as the forward-folding software used to create the observed temperature profiles. In § 4, we

combine our observational results with the theoretical predictions and discuss the implications of our results on the coronal heating problem as well as the agreement/disagreement with the Priest et al. (1998, 2000) and Aschwanden et al. (1999, 2000) results. In § 5, we review our conclusions.

2. OBSERVATIONS

CDS is a two-component, multichannel spectrometer on board *SOHO*, orbiting at the first Lagrangian point where it can observe the Sun continuously. The data archive was examined for images of quiescent loops on the limb that were reasonably isolated and had significant spectral coverage. The loop shown in Figure 1 was observed on 1998 April 20 at 20:54 UT and was selected as the best candidate available in the public domain at the time the data analysis began.

The CDS data are structured into cubes by scanning a slit across the Sun. Two spectra are generated at each pixel position, the first covering the wavelength range from 310 to 380 Å and the second covering 517–633 Å. It is rare that CDS will transmit data from the entire wavelength range back to Earth owing to limitations of telemetry. Instead, small wavelength bands, usually centered on strong emission lines, are transmitted. The emission lines included in this study are listed in Table 1. Thirteen pixels were chosen at positions along the length of the coronal loop shown in Figure 1, ranging from the southernmost footpoint, through the apex, and partly down the other side. The spectra were analyzed (13 pixels times 19 bands per pixel) using software available from the Solarsoft package. Baseline correction was performed by subtracting a zeroth-order polynomial from the overall spectra. Windows containing spectral background that could not be subtracted (usually because of a low signal-to-noise ratio) with any degree of confidence were disregarded. After subtraction, spectra were studied for possible blending in the lines. When no blends were evident, lines were fitted using a Gaussian profile, where the amplitude, the wavelength position of the peak, and the FWHM were varied to give the best fit to the data. Errors in the fit were calculated using both residual profiles and Poisson weighting statistics. We attempted to subtract background extreme ultraviolet (EUV) emission that was not part of the loop, but this emission is structured at cool temperatures ($\log T < 6.0$) and down by almost an order of magnitude in the temperature range of interest ($6.0 < \log T < 7.0$). Therefore, it should not affect our main results and a more detailed investigation of this background is left to a future paper.

SXT is one of four high-energy solar instruments on board *Yohkoh*, a spacecraft in low Earth orbit operated by a Japan/US/UK consortium. It is a broadband imaging instrument with multiple channels, designed originally to study flares, but it has made important contributions to less energetic aspects of solar physics as well. All stages of the data analysis were performed using Interactive Data Language software written and provided by SXT team members. The first step of the analysis was decompression, which transformed the data back to 12-bit and into units of data numbers per second. Then dark images (images of the

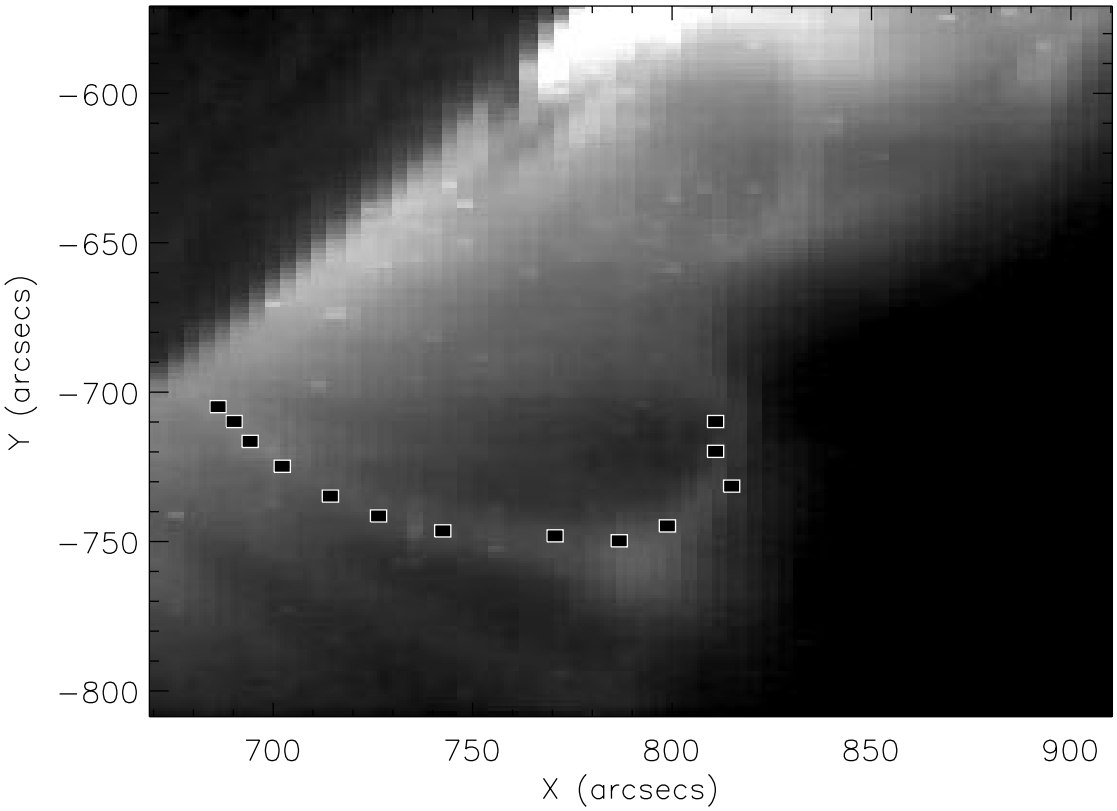

FIG. 1.—CDS image in Si XII at 520.66 Å observed on 1998 April 20 at 20:54 UT. The 13 highlighted pixels along the relatively isolated loop on the southwest limb of the solar disk were chosen for more in-depth analysis.

TABLE 1

CDS Spectral Line Intensities

Ion	Wavelength (Å)	log T	Pixel A	B	C	D	E	F	G	H	I	J	K	L	M
O v.....	629.73	5.40	253.	312.	286.	132.	74.8	14.8	11.2	9.76	5.60	8.30	...	80.5	144.
Ne vi.....	558.59	5.65	39.8	23.3	21.	28.4	...	6.83	10.7	30.2	4.60	31.3	...	...	...
Ca x	557.76	5.80	119.	87.4	99.9	70.	64.4	63.	54.8	47.	45.1	76.8	...	13.6	...
Mg ix	368.07	6.00	2582.	2327.	6814.	1440.	1212.	1444.	817.	388.	599.	140.1	708.	298.	671.
Mg x.....	624.94	6.05	596.	604.	499.	353.	287.	305.	210.	178.	195.	76.47	211.	109.	98.7
Si ix.....	341.94	6.05	421.	203.	170.	214.	52.	72.7	84.9	71.3	119.	149.	14.7	51.4	20.3
Fe xi	358.62	6.05	116.	482.	111.	88.3	171.	207.	181.	156.	78.2	256.	30.4	91.1	22.7
Si x.....	347.40	6.10	650.	650.	518.	387.	352.	235.	207.	128.	122.	31.4	51.7	72.6	110.
Si x.....	356.01	6.10	687.	636.	626.	608.	451.	417.	135.	...	151.	202.	100.	62.	192.
Al xi	568.12	6.15	57.2	95.9	110.	135.	29.9	73.6	68.2	67.	157.	64.7	52.1	32.1	140.
Al xi	550.03	6.15	95.5	86.7	97.1	70.2	...	40.4	37.3	31.2	35.7	50.6	35.7	23.6	27.3
Fe xii	346.85	6.15	205.	303.	175.	121.	115.	149.	57.9	89.4	127.	55.8	43.3	20.6	57.9
Fe xii	364.46	6.15	524.	514.	914.	359.	242.	231.	174.	139.	159.	164.	121.	83.2	128.
Fe xiii.....	359.64	6.20	295.	289.	288.	203.	168.	108.	106.	130.	123.	248.	107.	122.	131.
Fe xiii.....	348.18	6.20	267.	267.	243.	229.	187.	129.	112.	64.5	56.7	137.	75.6	54.5	111.
Si xii	520.66	6.25	385.	354.	405.	318.	259.	227.	205.	405.	249.	143.	175.	156.	285.
Fe xiv.....	353.83	6.25	213.	249.	414.	152.	179.	115.	111.	66.6	115.	106.	53.5	56.	124.
Fe xiv.....	334.17	6.25	520.	517.	525.	530.	334.	317.	345.	159.	292.	323.	184.	181.	256.
Fe xvi.....	360.76	6.40	1286.	932.	1177.	1108.	974.	932.	901.	908.	971.	952.	835.	822.	787.

Note.—Intensities are in units of ergs cm^{-2} s^{-1} sr^{-1}, and uncertainties are $\pm 10\%$.

dark current alone) were subtracted from the decompressed data, and the visible light contamination produced by a pinhole in the SXT entrance filter was removed. For our data, taken in the AlMgMn filter on 1998 April 20, the open fraction of the entrance filter is 0.3333. The final step in prepping for analysis was self-registration of the SXT data, i.e., aligning all exposures taken of our region to one another. In this case the first full-frame image taken within the CDS observing widow was chosen as a reference image. In all, four full-frame images were selected from the SXT data file sfr980420.2030, two with a short (0.168286 s) time exposure and two with a longer (5.36740 s) time exposure.

After both instruments were calibrated, coregistration procedures were performed to align the SXT and CDS data sets to one another. The first of these involved correcting for the difference in the mean distances to the Sun between CDS and SXT. Next, the relative roll angle and linear offset between the two instruments were measured by plotting full-frame overlays of SXT and EIT on *SOHO* and matching prominent solar structures on the limb and disk. A small roll angle of $\sim 0.^{\circ}03$ was present. The linear offset was $\sim 24.''5$ (solar Y-coordinates). All solar Y-coordinates for the SXT data were increased by this value. A final correction factor was multiplied into the integrated SXT intensities to account for the relative difference between CDS and SXT pixel sizes.

For each pixel, the data then included a set of calibrated CDS spectral line intensities and uncertainties (in ergs cm^{-2} s^{-1} sr^{-1}), as well as the calibrated SXT broadband measurement (in data numbers per second per full-resolution pixel) in the AlMgMn filter, which was used primarily to constrain the high-temperature end of the DEM curve (§ 3). Between these two instruments, observations within the range $\log T = 5.4$–7.0 are possible, with an appreciable overlap in temperature response allowing for investigation into cross-calibration factors between the instruments.

3. ANALYSIS

3.1. *Isothermal Approximation*

Under "coronal equilibrium" conditions of low-electron density and high excitation, the intensity I of a spectral line of wavelength λ_{ij} emitted at the Sun and measured at the Earth is given by

$$I(\lambda_{ij}) = \frac{1}{4\pi}\frac{hc}{\lambda_{ij}} A \int_0^L G(T) n_e^2 \, dl \, , \tag{1}$$

where the units of I are ergs cm^{-2} s^{-1} sr^{-1}, h is Planck's constant, c is the speed of light, A is the elemental abundance, n_e is the electron density in cm^{-3}, l is the line-of-sight element of length in centimeters, and L is the depth of the observing region. The temperature-dependent terms are often grouped together in what is called the contribution function, $G(T) = 0.8 A_i C_{ij}$, where 0.8 is the hydrogen abundance, A_i is the ionization fraction, and C_{ij} is the electron collision rate coefficient in photons cm^3 s^{-1}.

For many ions in the EUV, the $G(T)$ functions tend to peak sharply in temperature because of the strong temperature dependence of the ion fractions A_i and then fall off quickly to zero. This has led to a widespread simplification—an isothermal approximation—where the function can be replaced with its maximum value, i.e., the value of the $G(T)$ function at the peak formation temperature of the line. With this approximation, the $G(T)$ term can be extracted from the integral, leaving $\int n_e^2 \, dl$, the column emission measure (cm^{-5}), which gives a good indication of the amount of emitting plasma along the line of sight.

A somewhat more sophisticated isothermal approximation is used throughout solar coronal physics. This method involves taking a ratio of spectral lines (e.g., CDS, and the Flat Crystal Spectrometer on *Solar Maximum Mission*), of narrowband filters (e.g., EIT, *TRACE*), and

even of broadband filters (e.g., SXT). With spectral lines, the ideal case would use two lines of the same element, so the complicating factor of the elemental abundance will cancel out in the ratio. For example, using Fe XII at 346.85 Å to Fe XIV at 353.83 Å,

$$\frac{I_{346}}{I_{353}} = \frac{353}{346}\frac{G_{346}(T)}{G_{353}(T)}, \quad (2)$$

where the left-hand side of the equation represents the observed line intensity ratio and the right-hand side represents the theoretical intensity ratio as a function of temperature. The $G(T)$ functions for the CDS iron lines were calculated using information from version 2.0 of the CHIANTI atomic physics database (Dere et al. 1997) and the ionization fractions of Arnaud & Raymond (1992). The isothermal temperature is found at the value where the observed intensity ratio intersects the theoretical ratio function, as shown in Figure 2. We have used this approximation for several different iron ratios to compute the isothermal temperatures at each chosen pixel along the loop. Examples of these values are listed in Table 2. The 10% uncertainty on the spectral line intensities corresponds to a negligible temperature uncertainty because the theoretical $G(T)$ ratios are so steep in the temperature range of interest. Rather than quote these unphysical values, we adopt a more standard uncertainty of $\pm 5\%$.

Plots of these temperature values as a function of s, the arc distance along the loop, are shown in Figures 3*a* and 3*b*. It is striking how flat these curves are, reminiscent of the temperature distributions obtained by Lenz et al. (1999) using *TRACE* and Aschwanden et al. (1999, 2000) using EIT filter ratios. This is somewhat surprising because the CDS pixels are much larger (4.″064 × 4.″064) than either the EIT or *TRACE* pixels, and we had always assumed that there might be more than one loop in our field of view despite the appearance of the CDS image in Figure 1. If these temperature distributions were to hold up under greater scrutiny, the results would suggest that loop models such as those of Rosner, Tucker, & Vaiana (1978) would not apply to the CDS loop described here.

It is unfortunate that we cannot do a direct comparison of our CDS spectral line ratios with the narrowband filter

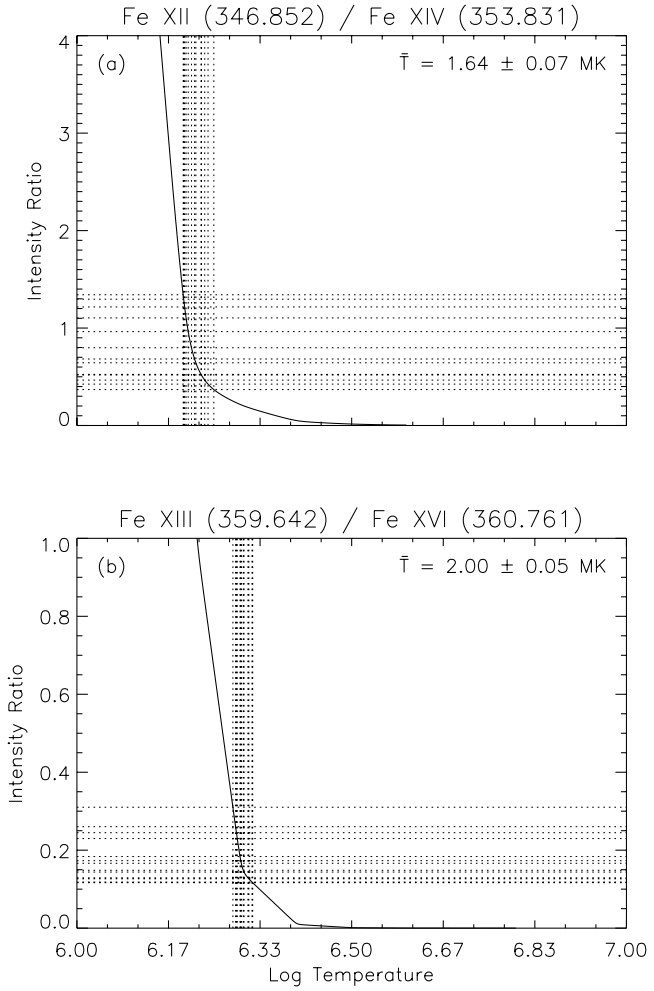

FIG. 2.—Two examples of the isothermal analysis. The intensity ratio of two iron lines is plotted against log T for (*a*) Fe XII λ346.852/Fe XIV λ353.831 and (*b*) Fe XIII λ359.642/Fe XVI λ360.761. In each case, the solid curve represents the theoretical intensity ratio taken from CHIANTI, the horizontal dashed lines depict the observed line intensity ratios from the 13 pixels (see Fig. 1), and the vertical dashed lines denote the intersection of each horizontal line with the theoretical curve, i.e., the temperature of the plasma at that pixel. Note that the mean temperatures obtained in (*a*) and (*b*) are statistically different.

TABLE 2

LOOP PLASMA PARAMETERS

Pixel	T_1[a] (mK)	T_2[a] (mK)	T_{DEM} (mK)	n_e (cm^{-3})	P (ergs cm^{-3})	E_r[b]	E_c[b]
A	1.59 ± 0.08	1.96 ± 0.10	1.20 ± 0.12	6 ± 0.5E9	2 ± 0.3	−7 ± 0.9E − 3	1.90 ± 0.19E − 4
B	1.57 ± 0.08	1.92 ± 0.10	1.10 ± 0.11	6 ± 0.5E9	2 ± 0.2	−7 ± 0.9E − 3	1.39 ± 0.14E − 4
C	1.73 ± 0.09	1.95 ± 0.10	1.15 ± 0.11	5 ± 0.5E9	2 ± 0.2	−5 ± 0.7E − 3	1.09 ± 0.11E − 4
D	1.62 ± 0.08	1.98 ± 0.10	1.66 ± 0.17	6 ± 0.5E9	3 ± 0.4	−6 ± 0.8E − 3	6.50 ± 0.65E − 5
E	1.65 ± 0.08	1.99 ± 0.10	1.74 ± 0.17	6 ± 0.5E9	3 ± 0.4	−6 ± 0.7E − 3	1.93 ± 0.19E − 5
F	1.56 ± 0.08	2.09 ± 0.10	1.91 ± 0.19	5 ± 0.5E9	3 ± 0.4	−4 ± 0.5E − 3	−9.33 ± 0.93E − 5
G	1.68 ± 0.08	2.08 ± 0.10	2.00 ± 0.20	4 ± 0.5E9	2 ± 0.4	−2 ± 0.4E − 3	−1.60 ± 0.16E − 4
H	1.56 ± 0.08	2.01 ± 0.10	2.09 ± 0.21	4 ± 0.5E9	2 ± 0.4	−2 ± 0.4E − 3	−1.75 ± 0.18E − 4
I	1.58 ± 0.08	2.06 ± 0.10	1.91 ± 0.19	4 ± 0.5E9	2 ± 0.3	−2 ± 0.4E − 3	−1.22 ± 0.12E − 4
J	1.68 ± 0.08	1.94 ± 0.10	2.09 ± 0.21	3 ± 0.5E9	2 ± 0.3	−1 ± 0.3E − 3	−1.28 ± 0.13E − 4
K	1.64 ± 0.08	2.05 ± 0.10	2.00 ± 0.20	3 ± 0.5E9	2 ± 0.3	−1 ± 0.3E − 3	−6.68 ± 0.67E − 5
L	1.77 ± 0.09	2.01 ± 0.10	1.91 ± 0.19	4 ± 0.5E9	2 ± 0.3	−2 ± 0.4E − 3	−3.01 ± 0.30E − 5
M.....	1.71 ± 0.09	1.99 ± 0.10	1.74 ± 0.17	5 ± 0.5E9	2 ± 0.3	−4 ± 0.6E − 3	−7.50 ± 0.75E − 7

[a] T_1 and T_2 were calculated from the ratios of Fe XII/Fe XIV and Fe XIII/Fe XVI, respectively.
[b] Radiative and conductive losses are in units of ergs cm^{-3} s^{-1}.

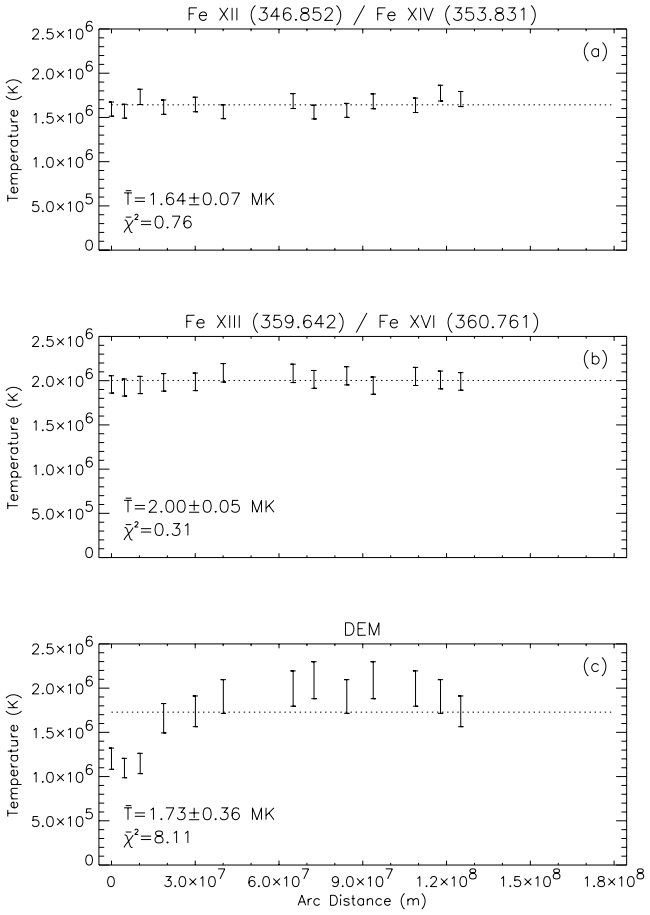

FIG. 3.—Temperature at each pixel as a function of arc distance along the loop. Results from the isothermal approximation from (*a*) Fig. 2*a* and (*b*) Fig. 2*b*, both with 5% error bars. In each case, a uniform temperature (*horizontal dashed line*) represents an excellent fit to the data. The points in (*c*) denote the peak temperatures from the 13 DEM curves, each with a 10% uncertainty. Note that a uniform temperature is a poor fit to the data.

ratios of either EIT or *TRACE*. But the coronal channels of these instruments are centered on Fe IX (171 Å), Fe XII (195 Å), and Fe XV (284 Å) lines, all with wavelengths below the CDS cutoff of 310 Å. In addition, there are no Fe IX or Fe XV lines in this CDS data set, so we cannot compare the results of another Fe IX/Fe XII or Fe XII/Fe XV line ratio. We do note, however, that the results depicted in Figures 3*a* and 3*b* are typical of the various iron intensity ratios available here—the temperatures are effectively uniform along the length of the loop.

There is, however, a problem with the isothermal approximation. The temperatures obtained from the various iron line ratios (for a given pixel) are statistically different. This is a strong indication that the plasma along the line of sight is multithermal. Therefore, in the next subsection, we drop the isothermal approximation and attempt to find the temperature distribution of the plasma along the lines of sight depicted in Figure 1.

3.2. *Multithermal Analysis*

There are many cases where the isothermal approximation does not produce a physically accurate representation of the emitting plasma. In this case we need to define the DEM, $Q(T)$ (Pottasch 1963; Withbroe 1975; Sylwester, Schrijver, & Mewe 1980), as

$$\int G(T)n_e^2\,dl = \int G(T)Q(T)dT\ , \tag{3}$$

where $Q(T) = n_e^2(dT/dl)^{-1}$ and represents the amount of emitting material as a function of temperature along the line of sight. The importance of understanding the multithermal nature of the plasma becomes apparent when one considers the tremendous variability in temperatures derived using techniques assuming isothermal plasma between flare and nonflare events, which may differ by orders of magnitude.

In practice, the DEM function must be determined through iterative comparison with observed line intensities. Rewriting the intensity integral in terms of the DEM and temperature, we arrive at the form used in this study:

$$I(\lambda_{ij}) = \frac{1}{4\pi}\frac{hc}{\lambda_{ij}}A\int_0^\infty G(T)Q(T)dT\ . \tag{4}$$

Since this equation is the line intensity for a particular spectral line, the range of temperatures must cover only the region immediately surrounding the line's peak formation temperature. This is a problem, considering that the true DEM curve should cover all temperatures in the emitting region, not just those around a particular line. In theory, one could input a wildly varying (even divergent) DEM function and still produce a realistic intensity, as long as the DEM in the general vicinity of the peak formation temperature can produce the desired result. The problem at hand then is one of constraint. To effectively test the validity of a DEM function, one needs several observed line intensities covering a wide temperature range. CDS data are ideal for this purpose.

The solid lines in Figure 4 show the emissivity functions for the CDS lines plotted as a function of temperature. These functions were calculated using the atomic physics from the CHIANTI database (Dere et al. 1997), the "hybrid" elemental abundances compiled by Fludra & Schmelz (1999), an electron density of 5×10^9 cm^{-3} (see Schmelz & Winter 1999), and the ionization fractions of Arnaud & Raymond (1992) for the iron lines and Arnaud & Rothenflug (1985) for all other lines. The figure shows the

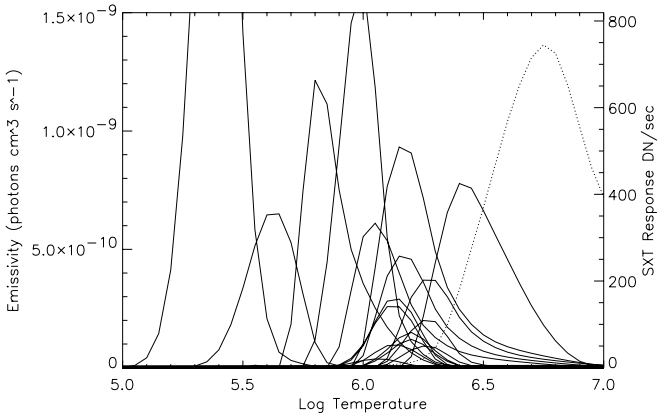

FIG. 4.—Emissivity functions for the CDS lines plotted as a function of temperature. The dotted curve shows the SXT response function for the AlMgMn filter. The combination of the data from these two instruments results in excellent temperature coverage in the range log T = 5.4–7.0.

good temperature coverage of the lines for the range log $T = 5.4$–6.5. The high-temperature value is probably not good enough for the study of active region loops. Therefore, in § 3.3, we introduce the SXT data needed to extend this range up to log $T = 7.0$ and beyond.

3.3. *Broadband Intensities*

Scattered results from various authors—Raymond & Foukal (1982) using EUV spectra from *Skylab*, Bruner et al. (1988) using XSST rocket data, Brickhouse, Raymond, & Smith (1995) and Brosius et al. (1996) using Solar EUV Rocket Telescope and Spectrometer (SERTS) data, and Schmelz et al. (1996) using X-ray data from *Solar Maximum Mission*—indicate that the emission measure distribution of quiescent coronal loops peaks around a temperature of 2–3 mK and falls off on either side. This structure has not been studied in detail, however, because so many instruments are sensitive either to the higher temperature portion of this peak (e.g., SXT and the Bragg Crystal Spectrometer on *Yohkoh*, the Flat Crystal Spectrometer on *Solar Maximum Mission*) or the lower temperature (e.g., EIT, SERTS, CDS, *TRACE*). Combining the data sets is the only way currently available to cover the full temperature range. There is sufficient overlap of the temperature responses of CDS and SXT to permit self-consistency checks as well as to do a detailed multithermal analysis with the combined data set where the SXT data are used primarily to constrain the high-temperature end of the distribution.

Calculating the theoretical total intensity from a broadband photon flux is considerably more difficult than for a single spectral line intensity as reviewed above, requiring integration over all wavelengths. The SXT team circumvents this problem by providing an instrument response function that gives the total signal in data numbers per second as a function of log T, assuming a constant (volume) emission measure of 10^{44} cm^{-3}. The response functions were derived by convolving a theoretical thermal spectrum with the instrumental effective area, defined as the product of the entrance filter transmission, mirror reflectivity, and CCD quantum efficiency. The theoretical spectrum used to generate the response functions assumed the adopted coronal abundances compiled by Meyer (1985) and the ion fractions calculated by Arnaud & Rothenflug (1985). The spectrum was altered for this study, namely, by inserting the hybrid elemental abundances provided by Fludra & Schmelz (1999) and the ionization fractions for iron calculated by Arnaud & Raymond (1992)—see Schmelz et al. (1999) for details. This altered response function is plotted in Figure 4 as the dotted curve.

To successfully apply multithermal analysis to the broadband intensity calculations, we must first unassume the constant emission measure inherent in the response function. This is done by dividing the response function by the constant emission measure, then multiplying by the DEM. The resulting total intensity is then

$$I \propto \int_0^\infty (\text{corrected response function}) \times Q(T)dT \ . \quad (5)$$

With the addition of the SXT data, our temperature coverage is extended from log $T = 6.5$ to log $T = 7.0$ and beyond. This results in a strong high-temperature constraint that allows for successful modeling of the thermal distribution of the loop using the forward-folding technique described in the next subsection.

3.4. *Forward Folding*

Forward folding is a standard technique used to determine a plasma emission measure distribution as a function of temperature. It requires an initial input model that is folded through the spectral line emissivity functions and broadband responses. This produces a set of predicted intensities that are compared with the observed values. The emission measure distribution is then adjusted iteratively (and subjectively) to improve the agreement between the observed and predicted intensities while keeping the curve as smooth a function of temperature as possible. The process is repeated until, ideally, most of the predicted and observed intensities agree to within approximately ± 1–$2\ \sigma$ of the observed values.

A DEM curve was generated for each of the 13 pixels shown in Figure 1. Each time, a flat curve with a log DEM value of 23.5 was used as the initial model for the forward-folding program. The program generated a set of predicted intensities for the CDS spectral lines listed in Table 1, as well as the SXT AlMgMn filter. The initial distribution was changed by small, iterative steps to bring the predicted data points as close as possible to the observed values. Figure 5*a* shows a typical example of the DEM curve and Figure 5*b* the predicted/observed intensity ratios for each of the CDS lines and the AlMgMn filter, all with 1 σ error bars, which

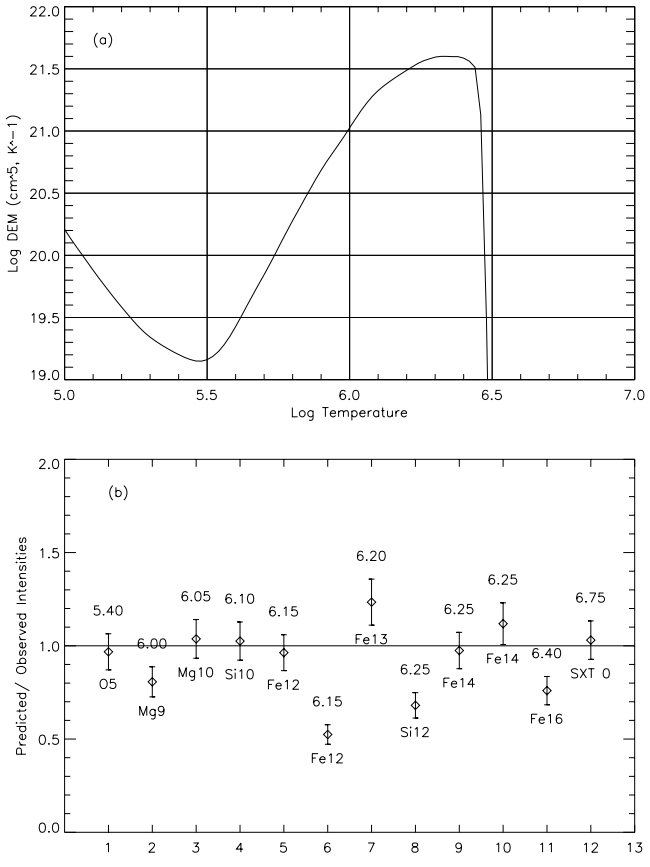

FIG. 5.—(*a*) DEM curve for pixel "H" near the top of the loop, showing the multithermal nature of the plasma along the line of sight. (*b*) The predicted-to-observed intensity ratio on a linear scale for the CDS spectral lines listed in Table 1, as well as the SXT broadband data for the AlMgMn filter. The numbers above each data point represent the log T of the peak formation temperature for each CDS line and the peak temperature of the SXT response curve.

depict the measurement uncertainty. Note the SXT data point on the far right-hand side of Figure 5*b*; all the other points represent CDS spectral lines.

Because the forward-folding process is subjective, we took several precautions to ensure that our personal biases were not represented in the DEM results. Chief among these precautions were the following:

1. The data sets for the 13 pixels (CDS line intensities plus coregistered AlMgMn broadband data) were scrambled by a colleague so we did not know the loop position of the pixel data we were working on. They were unscrambled only after the analysis was finished.
2. The forward-folding analysis was done independently by another colleague who was not told which data set was which until after he finished the analysis.

The original DEM analysis was done with an electron density of 5×10^9 cm^{-3}. But then we used a method first described by Schmelz & Winter (1999) to obtain a better value. We calculated the emissivity functions for 10 values of the density, 1, 2, 3...10 $\times 10^9$ cm^{-3}, and determined which set gives the lowest $\bar{\chi}^2$ in the error analysis plots (e.g., Fig. 5*b*). This method gives an accurate density value for the plasma in the pixel with a single significant figure (rather than a precise value with several significant figures obtained by other methods).

The resulting series of DEM curves is shown in Figure 6. The lowest curve (pixel A) represents the DEM distribution for the pixel closest to the southernmost footpoint (see Fig. 1), and the *y*-axis is calibrated for this point. Each subsequent curve (pixels B through M) shows the DEM distribution for the next pixel along the loop, rising from the southern leg, through the apex, and partway down the other side. Each curve is displaced from the one below it by half an order of magnitude on the *y*-scale.

There are several noteworthy features of the curves. First, the shape of the curves indicates that the plasma along the line of sight in each pixel cannot be considered isothermal. This is consistent with the different temperatures found from different iron line ratios using the isothermal approximation. It is possible that there is some contaminating material (i.e., plasma that is not confined to the loop) along the line of sight. This material is not obvious in the CDS images, but the CDS pixel size is rather large compared with the state-of-the-art spatial resolution of *TRACE*. If pixel size were the only factor, however, the CDS iron line ratios should not necessarily produce an isothermal loop. Another possible explanation is that the observed loop is made up of multiple strands of different temperatures, as suggested recently by Cargill & Klimchuk (1997) and Reale & Peres (2000). These results would certainly be consistent with our DEM curves, and we hope to do a more detailed comparison in a future paper.

The second feature of the DEM curves that deserves special mention is that the electron temperature at the peak of each curve in Figure 6 changes from curve to curve (from pixel to pixel). These temperatures are plotted in Figure 3*c* and show a distinctively different trend than the isothermal results depicted in Figures 3*a* and 3*b*. Not only is there a temperature distribution along the line of sight but along the loop as well. These peak temperatures, $T_{\rm DEM}$, and the electron densities, n_e, are listed in Table 2. These values are used to estimate the pressures, $P = 2n_e kT_{\rm DEM}$, at each pixel, where k is Boltzmann's constant.

The third point that needs to be made is that there is a significant amount of cool material (log $T < 6.0$) at each pixel, even at the top of the loop. In fact, there is detectable O V (peak formation temperature of log $T = 5.4$) for all pixels except the one labeled with the letter "K." There is obvious structure in the CDS O V image in and around our loop, so a simple "background subtraction" of this cool material is not feasible. We can say, however, that there is significant O V emission at about 8 scale heights above the southwest limb of the solar disk. In addition, the DEM curves in Figure 6 all turn up at the cool-temperature end. This is mainly to account for the O V emission. If the DEM curves did not turn up but continued downward with the same slope, the oxygen elemental abundance would have to be increased by up to a factor of 40 in order to account for the observed O V intensities.

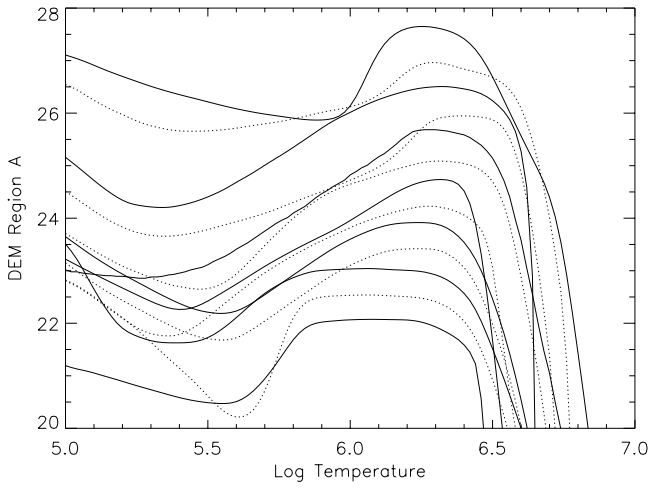

FIG. 6.—DEM curves for all 13 pixels (pixel A, *bottom*; pixel M, *top*), where the *y*-axis is calibrated to the bottom curve (pixel A), and each subsequent curve is offset by half an order of magnitude. The temperature distributions depicted here are not consistent with an isothermal approximation.

4. DISCUSSION

The mechanisms by which energy is transported into and dissipated inside the corona are unknown at present. However, there is an abundance of theoretical models proposed by many authors that are supported to some degree by observational data. Regardless of the model, any successful explanation of the source(s) of heating in the corona must answer three questions satisfactorily: (1) By what mechanism does the energy enter the corona? (2) How is the energy dissipated? and (3) Does this dissipation meet observed heating rates in the corona? Currently, none of the proposed models are without their detractors. It should also be noted that a combination of heating mechanisms is certainly possible, if not probable.

Following the procedure laid out in Rosner, Tucker, & Vaiana (1978) and Craig, McClymont, & Underwood (1978), we consider a steady state active region loop with a cross-sectional area $A(s)$ and half-length L; s is the arc length over the loop measured from some arbitrary base point, $s = 0$, and $L = 1.2 \times 10^{10}$ cm. Furthermore, let the plasma flow along the loop be zero, and the energy balance

between heating and conduction plus radiation be such that

$$E_H = -E_c - E_r , \tag{6}$$

where E_H is the volumetric heating rate from the (unspecified) heating mechanism, E_c is the conductive loss rate, and E_r is the radiative loss rate, all of which are in units of ergs cm^{-3} s^{-1}:

$$E_c = -\nabla \cdot \boldsymbol{F}_c = -\nabla \cdot (-\boldsymbol{\beta} \cdot \boldsymbol{E} - \boldsymbol{\kappa} \cdot \nabla \boldsymbol{T}) , \tag{7}$$

where $\boldsymbol{F}_c$ is the conductive heat flux in units of ergs cm^{-2} s^{-1} and the divergence is taken in the s-direction only. The first term on the right-hand side can be neglected under coronal conditions, and the second simplifies to $\kappa(dT/ds)$. The coefficient of conduction, κ, is defined as $\kappa_0 T^{5/2}$, where $\kappa_0 \approx 10^{-6}$ ergs cm^{-1} s^{-1} K$^{-7/2}$.

$$E_c = \frac{1}{A(s)} \frac{d}{ds} \left[A(s)\ \kappa_0\ T^{5/2}\ \frac{dT}{ds} \right] . \tag{8}$$

Since the variation in cross sections along our loop is relatively small (see, e.g., Klimchuk et al. 1992; Klimchuk 2000), $A(s)$ divides out of the above equation. Differentiating gives

$$E_c = \kappa_0 \left[T^{5/2}\ \frac{d^2T}{ds^2} + \frac{5}{2}\ T^{3/2}\ \left(\frac{dT}{ds}\right)^2 \right] . \tag{9}$$

For the radiative term

$$E_r = -Q(T)P(T)\ \frac{dT}{dl} , \tag{10}$$

where $Q(T)$ is the DEM, dT/dl is the temperature gradient along the line of sight, and $P(T)$ is the radiative loss function, i.e., the power emitted over all wavelengths per unit emission measure at a given temperature, with units of ergs cm^3 s^{-1}; $P(T)$ can be calculated for any set of coronal abundances and ion fractions, e.g., Cook et al. (1989) and J. Raymond (2000, private communication; see Fig. 3.12 of Golub & Pasachoff 1997). In the isothermal approximation, this simplifies to $E_r = -n_e^2 P(T)$, where n_e is the electron density.

Approximate values for E_r and E_c are listed in Table 2 for each pixel. The calculations for E_r used the value of the electron density obtained from the DEM curves and the radiative loss function computed with the hybrid elemental abundances (J. Raymond 2000, private communication). We quote only one significant figure for the E_r-values because the densities used to compute them are known only to this accuracy. The first and second derivatives for the E_c calculation were obtained by fitting a third-order polynomial to the temperature data plotted in Figure 3*c*. In each case, the required temperatures used were the values for the peak of each DEM curve, $T_{\rm DEM}$.

At first glance, it may seem inconsistent to assign a single temperature to each pixel after we have shown that there is multithermal plasma along each line of sight. It seems more likely that the observed loop is made up of multiple strands of different temperatures (e.g., Cargill & Klimchuk 1997; Reale & Peres 2000). The single temperature assigned to each pixel could reflect an average of many strands, so the model fit to the average temperatures would be equivalent to an average of many fits to the individual strands. This would be dangerous not only because the relative weighting of hot and cool strands could be different for the various pixels (Aschwanden & Nitta 2000) but also because the governing equations are highly nonlinear, so the solution to the average could be quite different from the average solution.

Assigning the temperature corresponding to the peaks of our DEM curves is somewhat better than using the temperatures from an isothermal approximation, however. The DEM curve temperatures listed in Table 2 represent the values for the bulk of the emitting plasma along that line of sight. By contrast, the isothermal approximation temperatures could be (and usually are) weighted heavily by the instrument response and may, therefore, represent a small fraction of the emitting material in a particular pixel. The results of this single-temperature comparison are not meant to be definitive but more like a first step to a more complex comparison that we have planned for a future paper.

The results listed in Table 2 show that we have a conductive gain rather than loss (positive terms) in the pixels closest to the southernmost footpoint. Traditionally, such a gain is expected in the transition region but not in the corona. But the data indicate that the second term in equation (9)—the positive term—dominates for these pixels. Our results also suggest that radiative losses are greater than conductive losses for this loop, which is contrary to the assumptions made by Priest et al. (1998, 2000). But the radiative losses do not necessarily overwhelm the conductive losses, which is contrary to the assumptions made by Aschwanden et al. (1999, 2000). Our results are in between these two extreme positions. Even though our radiative losses are higher than the conductive, they are, in fact, much closer to the original theoretical results of Rosner, Tucker, & Vaiana (1978), which expected comparable values for E_c and E_r in coronal loops.

5. CONCLUSIONS

Using simultaneous observations from the CDS and SXT instruments, DEM curves were calculated at various points along an active region coronal loop using a manual iterative method. The primary component necessary for successful application of this multithermal analysis technique to coronal plasmas, namely, a plethora of spectral lines covering a broad temperature range, were available from CDS. SXT served as a supporting instrument, primarily constraining the high-temperature end of the multithermal distribution.

Peak temperature values from the DEM curves were then used to construct the observed loop profile. This distribution showed a strong temperature gradient, in sharp contrast to the results obtained when an isothermal approximation was used. These results should serve as a strong warning to anyone using this simplistic method to obtain temperature. This warning is echoed on the EIT Web page that discusses the methods used to find temperature and emission measure. The page begins, "Danger! Enter at your own risk!" In other words, values for these parameters may be found, but they may not describe the observed plasma.

It is surprising to us that the isothermal approximation could mislead us so completely. There is no doubt that we would have concluded that $dT/ds \approx 0$ and that the conductive losses were so small compared with the radiative losses that we could neglect them. The results from the multithermal analysis lead to a different conclusion: dT/ds is

significant and, therefore, conductive losses should not be ignored. Our results suggest that the assumptions made by Priest et al. (1998, 2000)—that conductive losses dominate—and those made by Aschwanden et al. (1999, 2000)—that radiative losses dominate—are not appropriate for this particular loop.

We hope to compare our observational results with more complex theoretical models such as those described by Walsh (1999) and Klimchuk & Cargill (2001) that can address the multithermal nature of the plasma. We also want to investigate possible abundance deviations from standard published values, incorporate EIT and/or *TRACE* data into our analysis, and expand this study to other loops.

Solar physics research at the University of Memphis is supported through NASA grants NAG5-7197 and NAG5-9783. It is a pleasure to thank University of Memphis physics students C. R. Edwards and D. A. Medlin for their assistance with data analysis.

REFERENCES

Arnaud, M., & Raymond, J. 1992, ApJ, 398, 394
Arnaud, M., & Rothenflug, R. 1985, A&AS, 60, 425
Aschwanden, M. J., Alexander, D., Hurlburt, N., Newmark, J. S., Neupert, W. M., Klimchuk, J. A., & Gary, G. A. 2000, ApJ, 531, 1129
Aschwanden, M. J., Newmark, J. S., Delaboudinière, J.-P., Neupert, W. M., Klimchuk, J. A., Gary, G. A., Portier-Fozzani, F., & Zucker, A. 1999, ApJ, 515, 842
Aschwanden, M. J., & Nitta, N. 2000, ApJ, 535, L59
Brickhouse, N. S., Raymond, J. C., & Smith, B. W. 1995, ApJS, 97, 551
Brosius, J. W., Davila, J. M., Thomas, R. J., & Monsignori-Fossi, B. C. 1996, ApJS, 106, 143
Bruner, M. E., et al. 1988, J. Phys. C, 49, 115
Cargill, P. J., & Klimchuk, J. A. 1997, ApJ, 478, 799
Cook, J. W., Cheng, C.-C., Jacobs, V. L., & Antiochos, S. K. 1989, ApJ, 338, 1176
Craig, I. J. D., McClymont, A. N., & Underwood, J. H. 1978, A&A, 70, 1
Dere, K. P., Landi, E., Mason, H. E., Monsignori Fossi, B. C., & Young, P. R. 1997, A&AS, 125, 149
Fludra, A., & Schmelz, J. T. 1999, A&A, 348, 286
Golub, L., & Pasachoff, J. M. 1997, The Solar Corona (Cambridge: Cambridge Univ. Press)
Kano, R., & Tsuneta, S. 1996, PASJ, 48, 535
Klimchuk, J. A. 2000, Sol. Phys., 193, 53
Klimchuk, J. A., & Cargill, P. J. 2001, ApJ, 553, 440
Klimchuk, J. A., Lemen, J. R., Feldman, U., Tsunata, S., & Uchida, Y. 1992, PASJ, 44, L181
Klimchuk, J. A., & Porter, L. J. 1995, Nature, 377, 131
Lenz, D. D., DeLuca, E. E., Golub, L., Rosner, R., & Bookbinder, J. A. 1999, ApJ, 517, L155
Mandrini, C. H., Demoulin, P., & Klimchuk, J. A. 2000, ApJ, 530, 999
Meyer, J.-P. 1985, ApJS, 57, 173
Pottasch, S. R. 1963, ApJ, 137, 945
Priest, E. R., Foley, C. R., Heyvaerts, J., Arber, T. D., Culhane, J. L., & Acton, L. W. 1998, Nature, 393, 545
Priest, E. R., Foley, C. R., Heyvaerts, J., Arber, T. D., Mackay, D., Culhane, J. L., & Acton, L. W. 2000, ApJ, 539, 1002
Raymond, J. C., & Foukal, P. 1982, ApJ, 253, 323
Reale, F., & Peres, G. 2000, ApJ, 528, L45
Rosner, R., Tucker, W. H., & Vaiana, G. S. 1978, ApJ, 220, 643
Schmelz, J. T., Saba, J. L. R., Ghosh, D., & Strong, K. T. 1996, ApJ, 473, 519
Schmelz, J. T., Saba, J. L. R., Strong, K. T., Winter, H. D., & Brosius, J. W. 1999, ApJ, 523, 432
Schmelz, J. T., & Winter, H. D. 1999, in Proc. 8th *SOHO* Workshop: Plasma Dynamics and Diagnostics in the Solar Transition Region and Corona, ed. J.-C. Vial & B. Kaldeich-Schurmann (ESA SP-446; Noordwijk: ESA), 593
Sturrock, P. A., Wheatland, M. S., & Acton, L. W. 1996, ApJ, 461, L115
Sylwester, J., Schrijver, J., & Mewe, R. 1980, Sol. Phys., 67, 285
Walsh, R. W. 1999, in Proc. 8th *SOHO* Workshop: Plasma Dynamics and Diagnostics in the Solar Transition Region and Corona, ed. J.-C. Vial & B. Kaldeich-Schurmann (ESA SP-446; Noordwijk: ESA), 81
Withbroe, G. L. 1975, Sol. Phys., 45, 301